

## **Optical and Quantum Communications**

### **RLE Group**

Optical and Quantum Communications Group

### **Academic and Research Staff**

Professor Jeffrey H. Shapiro, Dr. Franco N. C. Wong, Dr. Dmitry Kolker, Dr. Mohsen Razavi

### **Graduate Students**

Baris I. Erkmén, Saikat Guha, Taehyun Kim, Onur Kuzucu, Dheera Venkatraman

### **Visiting Graduate Student**

Ingo Stork genannt Wersborg

### **Undergraduate Student**

Chen Li

The central theme of our programs has been to advance the understanding of optical and quantum communication, radar, and sensing systems. Broadly speaking, this has entailed: (1) developing system-analytic models for important propagation, detection, and communication scenarios; (2) using these models to derive the fundamental limits on system performance; and (3) identifying, and establishing through experimentation the feasibility of, techniques and devices which can be used to approach these performance limits.

## **1. Quantum Information and Communication**

### **Sponsors**

Air Force Research Laboratory Contract FA8750-06-2-0069

Army Research Office – Grant W911NF-05-1-0197

U.S. Department of Interior Contract NBCHC060072

U.S. Department of Interior Contract NBCHC00671

HP-MIT Alliance

NIST - Grant 60NANB5D1004

NIST - Grant 60NANB5D1115

NIST - Grant 70NANB7H6002

Office of Naval Research - Contract N00014-02-1-0717

### **Project Staff**

Professor Jeffrey H. Shapiro, Dr. Franco N. C. Wong, Dr. Mohsen Razavi

Baris I. Erkmén, Saikat Guha, Taehyun Kim, Onur Kuzucu, Ingo Stork genannt Wersborg,

Dheera Venkatraman, Chen Li

We are embarked on research in the area of quantum information technology whose goal is to enable the quantum-mechanical information transmission, storage, and processing needed for future applications in quantum computing and quantum communication. Our theoretical work in this area has focused on architectural designs for long-distance teleportation and multi-party entanglement transmission, and on novel applications of entanglement. Of particular interest has been the identification of high-performance means for generating the polarization-entangled photons needed for many quantum information applications, including teleportation, entanglement-based quantum positioning and clock synchronization, and quantum secret sharing. We are also interested in the fundamental limits on classical information transmission that are due to the quantum noise of bosonic channels. Our main experimental work is focused on generation and application of entanglement sources with high brightness and wavelength

tunability. In addition, we are interested in novel entanglement sources and their applications in quantum logic gates, enhanced quantum measurements, and quantum teleportation protocols.

Architectural Analysis The preeminent obstacle to the development of quantum information technology is the difficulty of transmitting quantum information over noisy and lossy quantum communication channels, recovering and refreshing the quantum information that is received, and then storing it in a reliable quantum memory. We led a team of researchers from MIT and Northwestern University (NU) that proposed, analyzed, and worked to develop the key technological elements of a novel architecture for the singlet-state approach to quantum teleportation [1,2]. A simple block diagram of this architecture is shown in Fig. 1. It consists of an ultrabright narrowband source of polarization-entangled photons pairs ( $P$ ), connected to a pair of trapped Rb atom quantum memories ( $M$ ) by transmission through  $L$ -km-long lengths of standard telecommunication fiber.



**Figure 1.** Schematic of long-distance quantum communication system:  $P$  = ultrabright narrowband source of polarization-entangled photon pairs;  $L$  =  $L$  km of standard telecommunication fiber;  $M$  = trapped atom quantum memory.

Each  $M$  block in Fig. 1 is a quantum memory in which a single ultracold  $^{87}\text{Rb}$  atom is confined by a  $\text{CO}_2$ -laser trap in an ultra-high vacuum chamber with cryogenic walls within a high-finesse single-ended optical cavity. An abstract representation of the relevant hyperfine levels for such a memory is given in Fig. 2(a). A 795 nm photon in an arbitrary polarization can be absorbed, transferring the qubit from the photon to the degenerate  $B$  levels of Fig. 2(a), and thence to long-lived storage levels, by coherently driving the  $B$ -to- $D$  transitions. By means of optically-off-resonant (OOR) transitions, the Bell states of two atoms in a single vacuum-chamber trap can be converted into superposition states of one of the atoms. All four Bell measurements needed for the Bennett *et al.* singlet-state teleportation process [3] can then be made, sequentially, by detecting the presence (or absence) of fluorescence as an appropriate sequence of OOR laser pulses is applied to the latter atom. The Bell-measurement results (two bits of classical information) in one memory can be sent to a distant memory, where (at most) two additional OOR pulses are needed to complete the state transformation process. More details on this memory, and its use in teleportation, are given in [4].

The  $P$  block in Fig. 1 is an ultrabright narrowband source of polarization-entangled photon pairs [5], capable of producing  $\sim 10^6$  pairs/sec in  $\sim 30$  MHz bandwidth by appropriately combining the signal and idler output beams from two doubly-resonant type-II phase matched optical parametric amplifiers (OPAs), as sketched in Fig. 2(b). The importance of our resonant approach to entanglement generation is the need to achieve high flux within the narrow linewidth of the Rb atom memory; existing parametric downconverter sources of entanglement are far too broadband to permit useful transmission rates in the Fig. 1 architecture.

Our previous performance analysis [1,6] for the MIT/NU teleportation architecture employed cold-cavity techniques, i.e., the success probability for loading the desired singlet state into the two memories shown in Fig. 1 was found by neglecting the presence of intracavity atoms and merely calculating the probability that — at the end of a loading interval — the photon fields inside the memory cavities are in the singlet state. During the past year we have remedied the deficiency of neglecting the intracavity atoms in assessing the MIT/NU teleportation architecture [7,8]. A summary of the results we obtained is as follows.

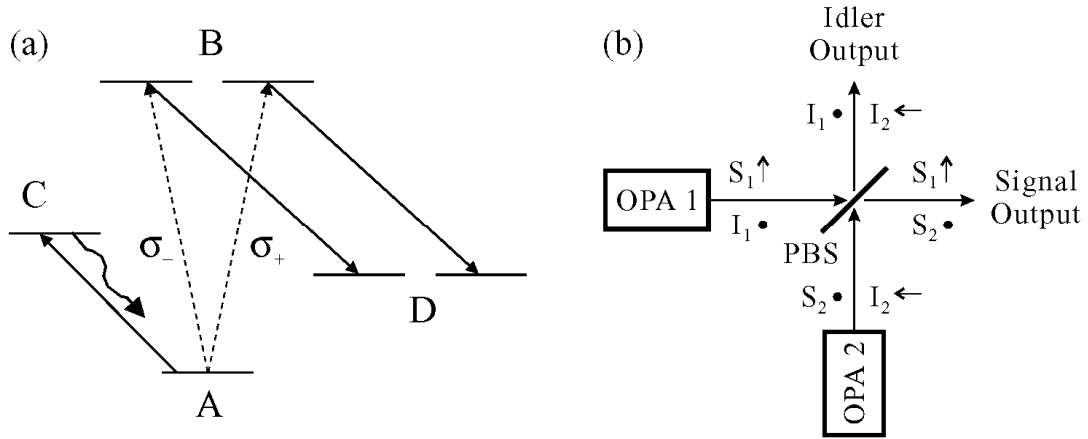


**Figure 2.** Essential components of singlet-state quantum communication system from Fig. 1. Left (a), simplified atomic-level schematic of the trapped Rb atom quantum memory: *A*-to-*B* transition occurs when one photon from an entangled pair is absorbed; *B*-to-*D* transition is coherently driven to enable storage in the long-lived *D* levels; *A*-to-*C* cycling transition permits nondestructive determination of when a photon has been absorbed. Right (b), ultrabright narrowband source of polarization-entangled photon pairs: each optical parametric amplifier (OPA1 and OPA2) is type-II phase matched; for each optical beam the propagation direction is *z*, and *x* and *y* polarizations are denoted by arrows and bullets, respectively; PBS, polarizing beam splitter.

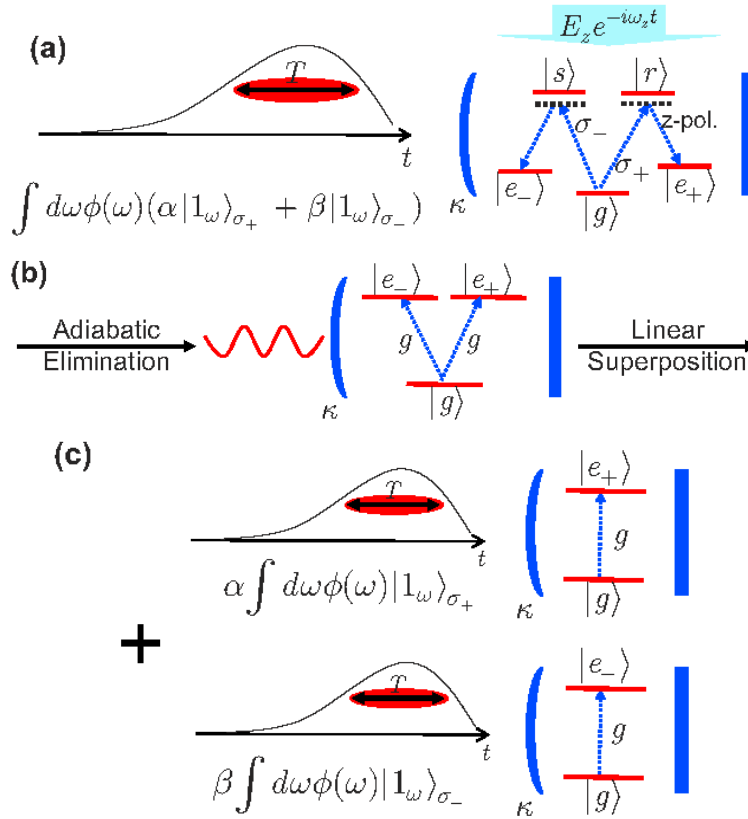


**Figure 3.** (a) Loading a double- $\Lambda$  atom driven by a polarization-state single photon. By adiabatically eliminating the upper states, this system becomes equivalent to the V-level system shown in (b); (c) Reduction of the V-level loading problem to two two-level loading problems by linear superposition.

We have developed a system-reservoir theory for trapped-atom memory loading and applied that theory to obtain analytical loading efficiency expressions for two-level, V-level,  $\Lambda$ -level and double- $\Lambda$ -level atomic configurations. It turned out that all of these configurations could be reduced to equivalent two-level problems [8]. In particular, for the double- $\Lambda$ -level configuration, shown in Fig. 3(a), which models the MIT/NU architecture's quantum memory, adiabatic elimination makes this system equivalent to the V-level configuration shown in Fig. 3(b). Linear superposition then permits the V-level loading problem to be reduced to a pair of two-level configuration loading problems, as shown in Fig. 3(c). We have proposed and evaluated a new off-resonant nonadiabatic approach to loading a  $\Lambda$ -level atom, and compared its performance to that of the well-known adiabatic transfer technique [9]. Figure 4 shows the optimum coupling rate  $g_c$  and the maximum loading probability achieved at this rate for both the adiabatic and nonadiabatic approaches plotted as functions of  $\kappa T$ , where  $\kappa$  is the cavity decay rate and  $T$  is the effective duration of the hyperbolic-secant single-photon input pulse. Whereas the adiabatic loading scheme has a constraint on its permissible pulse width, no such constraint exists for our nonadiabatic approach. Thus, as seen in Fig. 4, the latter can be used with a broader range of input-pulse time durations, which permits more convenient larger cavities to be employed.

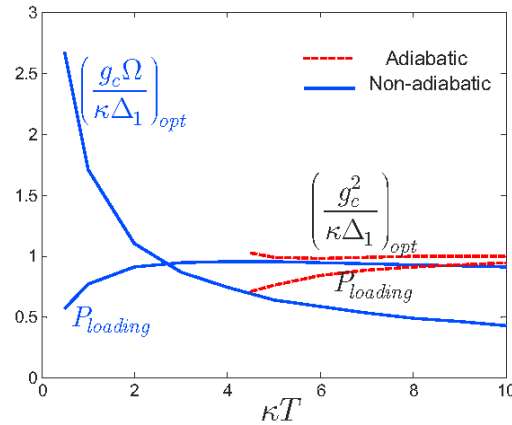


**Figure 4.** The optimum coupling rate and maximum loading probability achieved at this rate for both adiabatic and nonadiabatic approaches. For details see [8].

Figure 4 shows that nonadiabatic loading can achieve very high loading probabilities for a single-photon pulse illuminating an MIT/NU architecture quantum memory. Of greater importance, for evaluating the performance of the MIT/NU teleportation architecture, is the probability for a singlet state to load a pair of MIT/NU architecture quantum memories. As shown in Fig. 5(a), the relevant loading calculation involves two double- $\Lambda$  atoms illuminated by a polarization-entangled biphoton. This loading problem can be decomposed into two simpler loading problems, each involving an entangled photon illuminating a  $\Lambda$ -level atom, see Fig. 5(b). By means of adiabatic elimination, each Fig. 5(b) can be further reduced to one in which an entangled biphoton illuminates a pair of two-level atoms, as shown in Fig. 6. Again exploiting linear superposition, we have solved the Fig. 6 problem, obtaining the results shown in Fig. 7 for the optimum coupling rate  $g$  and the loading probability at that optimum coupling rate as functions of  $\kappa T$  and  $\kappa T_0$ , where  $T_0$  is the signal/idler time dispersion of the parametric downconverter used to generate the biphoton [8]. Figure 7 shows that our nonadiabatic loading scheme can achieve loading probabilities as high as 0.7 to 0.8. Adiabatic loading can, in principle, achieve perfect loading (probability  $\approx 1$ ), but, as noted earlier, it is more restricted in the pulse durations (input bandwidths) and cavity sizes that can be employed.

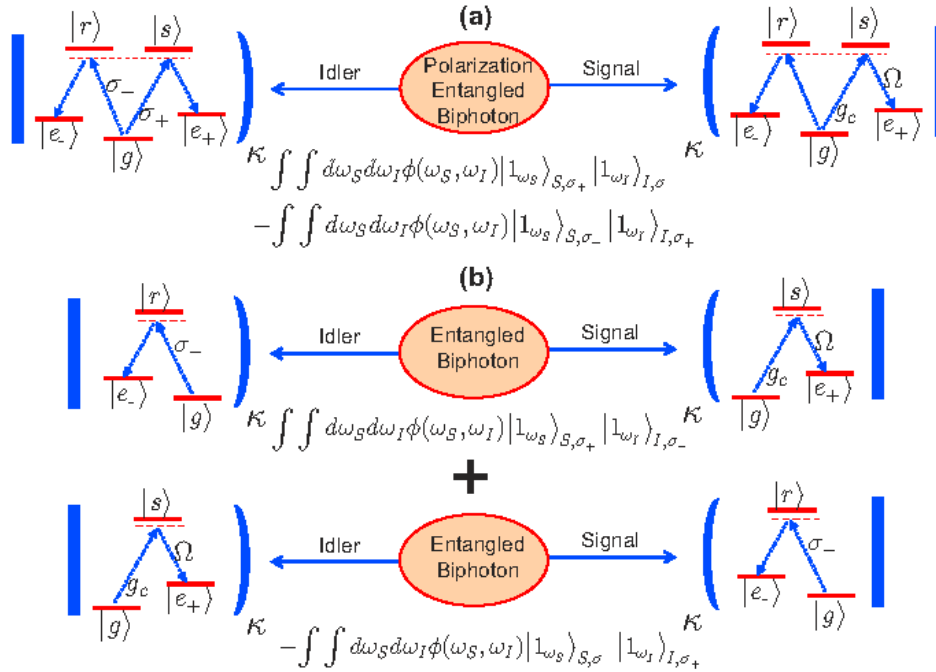


**Figure 5.** (a) Loading a pair of double- $\Lambda$  atoms illuminated by a polarization-entangled biphoton. (b) Breaking the loading problem from (a) into two simpler loading problems for a pair of  $\Lambda$ -level atoms, each illuminated by a biphoton state.

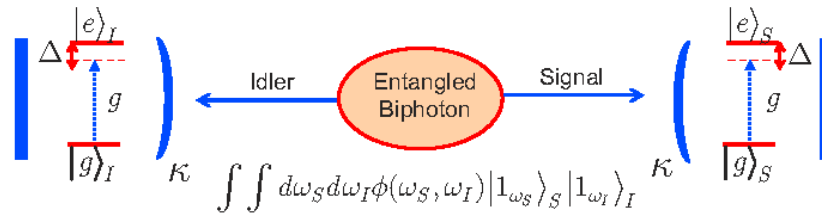


**Figure 6.** A two-level atom model for the systems shown in Fig. 5. For details see [8]

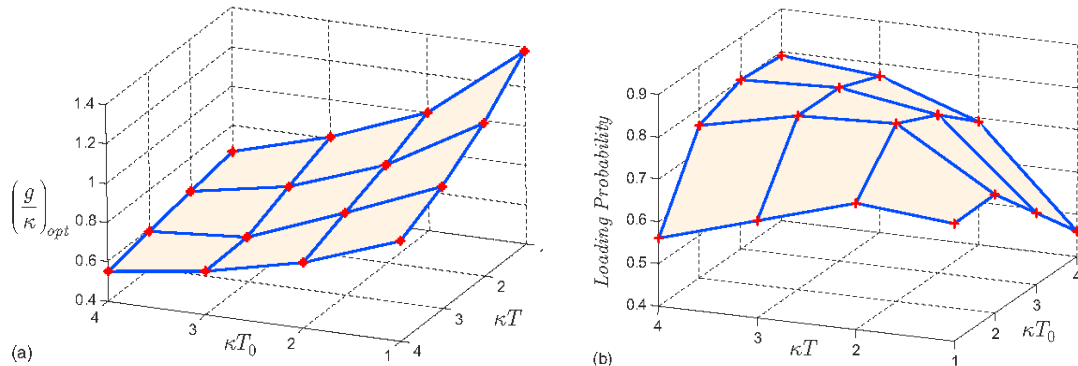


**Figure 7.** (a) the optimum normalized coupling rate versus normalized pulse length and normalized downconverter dispersion for the MIT/NU nonadiabatic loading problem. (b) The maximum loading probability at the optimum normalized coupling rate. For details see [8].

**High-Flux Polarization Entanglement Source** In recent years most entanglement sources have been based on spontaneous parametric downconversion (SPDC) in a noncollinearly propagating, angle phase-matched crystal, such as beta barium borate (BBO) [10]. We have taken a different approach to entanglement generation that takes advantage of advances in nonlinear materials and utilizes standard techniques in nonlinear optics. We employ the method of quasi-phase matching in periodically-poled potassium titanyl phosphate (PPKTP) or periodically-poled lithium niobate (PPLN) to enable efficient downconversion at user-specified wavelengths. In addition, collinear propagation of the pump, signal, and idler fields ensure easy manipulation and optimal collection of the output light. Recently we have developed the bidirectionally pumped polarization Sagnac interferometer, as shown in Fig. 8, that yields phase-stable polarization-entangled photons with high brightness and high fidelity [11].

In a typical polarization Sagnac configuration, we use type-II phase-matched PPKTP as the nonlinear crystal in a compact setup that does not require spatial, spectral, or temporal filtering. A 10-mm-long PPKTP crystal with a  $\sim 10\text{-}\mu\text{m}$  grating period is pumped by a fiber-coupled continuous-wave (cw) ultraviolet (UV) laser at 405 nm for generating polarization entanglement at 810 nm. The pump enters the Sagnac interferometer through a dual-wavelength polarizing beam splitter (PBS), which separates the pump light into its horizontal ( $H$ ) and vertical ( $V$ ) polarization components. The relative amplitude and phase between the pump's  $H$  and  $V$  components are set by the half-wave plate (HWP) and quarter-wave plate (QWP) placed before the interferometer. The Sagnac configuration, with counter-propagating beams traveling the same paths, eliminates the need for pump phase stabilization that was needed in the first-generation bidirectional pumping setup using a Mach-Zehnder interferometer [12].

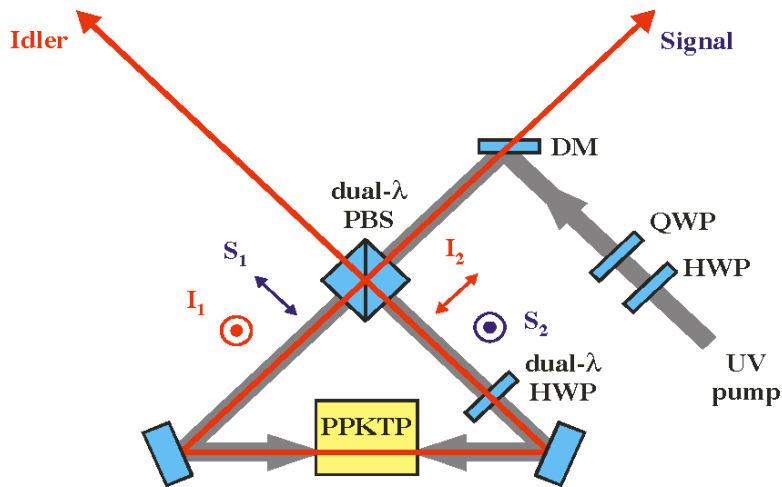


**Figure 8.** Schematic of bidirectionally-pumped SPDC in a Sagnac interferometer configuration. The dual-wavelength PBS combines the two downconverted outputs to form polarization-entangled signal and idler beams that may have different wavelengths. The relative amplitude and phase of the pump's  $H$ - and  $V$ -polarized components are set by the HWP and QWP. HWP, half-wave plate; QWP, quarter-wave plate; PBS, polarizing beam splitter; DM, dichroic mirror.

The PPKTP crystal is set up for frequency-degenerate type-II phase matching with orthogonally polarized signal and idler outputs. The dual-wavelength HWP rotates the  $V$ -polarized pump component to be  $H$ -polarized, along the crystal's  $y$  axis, which is required for SPDC in PPKTP. Bidirectional pumping thus effectively creates two identical coherently-pumped downconverters. We rotate the outputs of one of the beams by  $90^\circ$  with the dual-wavelength HWP, and combine the two downconverted beams at the dual-wavelength PBS, whose outputs are polarization entangled independent of the output frequencies and propagation directions. We have effectively engineered a decoherence-free subspace in which all output photon pairs are polarization

entangled. There is complete indistinguishability (spatially, spectrally, and temporally) at the output. This makes it impossible to tell from which downconverter an output photon originates. Hence the output from the Fig. 8 setup is a coherent superposition of the two downconverted beams [5]. The state of the polarization-entangled output is given by

$$|\psi\rangle = \left( |H\rangle_1 |V\rangle_2 - e^{i\phi} |V\rangle_1 |H\rangle_2 \right) / \sqrt{2},$$

where the phase  $\phi$  is equal to the pump phase set by the pump's HWP and QWP, plus a fixed offset phase that is related to material dispersion in the interferometer. As a result, the state of the output can be precisely controlled by simply changing the relative phase between the  $H$ - and  $V$ -polarized components of the pump input.

Figure 9 shows the earlier [11] and latest [13] results of two-photon quantum interference measurements for the Sagnac SPDC source output, plotting the spectral brightness as a function of the two-photon quantum interference visibility. The higher spectral brightness is obtained at a larger collection aperture size that also introduces spatial distinguishability, thus degrading the quantum-interference visibility. We have also measured the Clauser, Horne, Shimony, and Holt (CHSH) form of Bell's inequality violation [14], obtaining a value of  $2.8253 \pm 0.015 \pm 0.0035$  for the  $S$  parameter [13], which is a strong violation of the classical limit of 2 and very close to the quantum limit of  $2\sqrt{2}$ . The first standard deviation of  $S$  is that due to systematic errors while the second standard deviation is statistical. This compact and phase-stable Sagnac source may prove to be useful for many quantum optical applications, such as quantum key distribution and linear optics quantum computing. We also intend to use the Sagnac source for the generation of hyperentangled photons that are entangled in both momentum and polarization degrees of freedom.

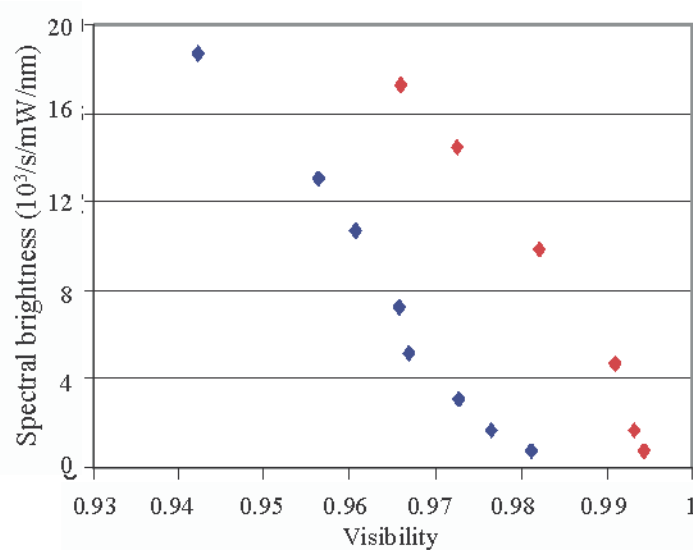


**Figure 9.** Comparison of spectral brightness of Sagnac source as a function of achievable two-photon interference visibility for earlier setup (blue diamonds) [11] and improved setup (red diamonds) [13].

More recently, we have developed a high-flux, pulsed, narrowband polarization entanglement source based on the same Sagnac configuration but with a narrowband pulsed pump. A pulsed source of polarization-entangled photons is well suited for free-space quantum key distribution because it provides temporal discrimination against background light. In order to generate sufficient entangled pair flux, we have first developed a narrowband pump source at 390 nm by frequency quadrupling of an amplified erbium-doped fiber laser at 1561 nm [15].

Our UV source design uses a compact modelocked fiber laser and a high-power polarization maintaining (PM) erbium-doped fiber amplifier (EDFA), followed by two second-harmonic generation (SHG) stages using MgO-doped periodically poled lithium niobate (MgO:PPLN) in the first stage and periodically poled KTiOPO<sub>4</sub> (PPKTP) in the second stage. We built a passively modelocked fiber laser with a saturable absorbing mirror and used a 25-GHz-wide fiber Bragg grating centered at 1561.4 nm for intracavity filtering, as shown in Fig. 10. A 90-cm-long highly doped erbium gain fiber was pumped with a 980-nm diode pump laser through a wavelength division multiplexing (WDM) combiner. Passive modelocking was accomplished by using a commercial intracavity saturable absorber mirror with 25% saturable loss. The output was coupled out and sent into an inline fiber polarization controller followed by a fiber polarization splitter, which converted the non-PM output of the fiber laser into two orthogonally polarized modes in two PM fibers. At a pump power of 290 mW, we obtained 1.8 mW cw modelocked output power from one of the PM output ports, with a pulse repetition rate of ~31 MHz. Even though the fiber laser used non-PM components, the output power level was stable over long periods of time without any manual adjustments. (Note that we have recently demonstrated a PM version of the picosecond fiber laser that eliminates the need for polarization control [16].) The output of the fiber laser was sent to an IPG Photonics multi-stage, PM EDFA with 5 W of saturated output power and a polarization extinction ratio greater than 17 dB.

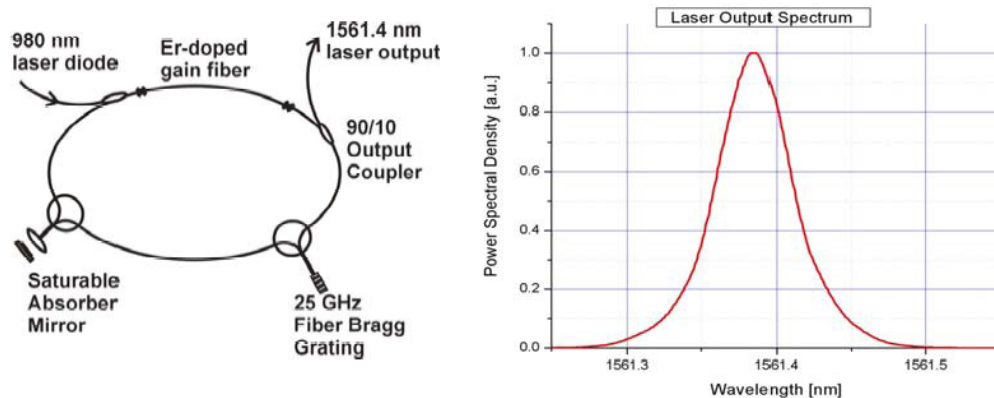


**Figure 10.** Schematic of a passively modelocked fiber laser in a ring configuration (left panel) and output spectrum centered at 1561.4 nm with a measured 3-dB bandwidth of 0.06 nm (right panel).

For the first frequency doubling stage, we used a 10-mm long MgO:PPLN crystal with a grating period of 19.5  $\mu\text{m}$  at an operating temperature of 93.7°C for type-I phase matching. Figure 11(a) shows a pulsed SHG conversion efficiency of over 60% for input pump powers above 3 W with a maximum efficiency of 68%. We made an intensity autocorrelation measurement of the fiber laser output, showing a pulse duration of 75 ps. A similar measurement for the first SHG output at 2 W average output power indicated a pulse width of 49 ps. We note that the output at 780.7 nm had a spatial mode that was very close to an ideal TEM<sub>00</sub>-mode with negligible ellipticity. For the second SHG stage, we chose to use a 14-mm long uncoated hydrothermally grown PPKTP crystal with a grating period of 7.65  $\mu\text{m}$ . Type-II phase matching at an operating temperature of 94.6°C was used to generate a TEM<sub>00</sub>-mode output with an average power of 250 mW from 2.8 W of 780.7-nm light, which represents a 5.5% frequency quadrupling efficiency. Figure 11(b) is a time trace of the UV output power over a 60-minute duration, showing some initial thermally-induced fluctuations in the short term followed by a long-term stable output. We note that with proper antireflection coating and a better quality PPKTP crystal, we have obtained an output power of over 400 mW.

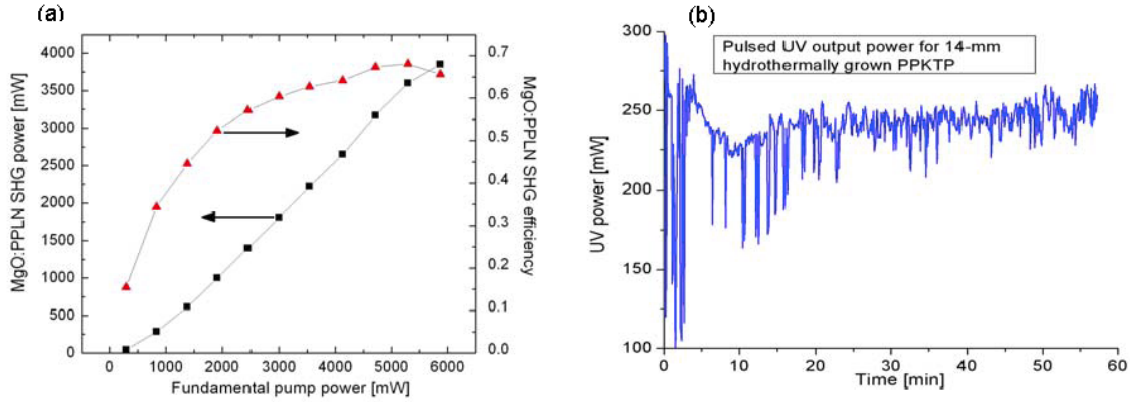


**Figure 11.** (a) Plot of first-stage second-harmonic 780.7-nm output power and conversion efficiency as a function of the input pump power. (b) Time trace of second-stage second-harmonic output at 390.35 nm.

We used the narrowband ( $<0.1$  nm) pulsed source to pump a parametric downconverter that was configured in the Sagnac geometry with a 10-mm-long PPKTP crystal whose grating period was  $7.85 \mu\text{m}$ . Figure 12 shows a picture of the Sagnac setup, the incoming pump beam path, and the two output beam paths. The incoming UV pump beam was filtered to remove residual 780.7-nm light with a 7-pass dichroic mirror pair that provided 140 dB suppression. Because of the high efficiency of the Sagnac configuration, we only needed an average pump power of 1 mW to generate a 1% entangled pair generation probability per pulse. This represents a new regime of entanglement generation in which we are capable of generating pairs at a significantly higher pair generation rate than cw operation. Indeed, we have been able to reach beyond a 50% generation rate per pulse, limited only by the possibility of UV-induced damage to the PPKTP crystal.

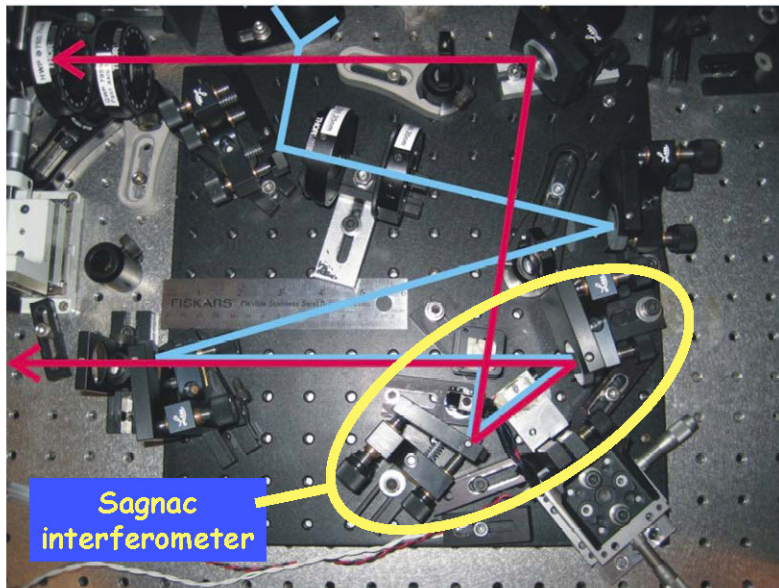


**Figure 12.** Photograph of the pulsed Sagnac source setup, showing the beam paths taken by the UV pump beam (blue) and by the near-infrared signal and idler outputs.

At high mean photon-pair generation rates, the Poisson distribution of the parametric downconversion process dictates that the multiple pair generation events are no longer negligible. These multi-pair events may create errors in quantum information processing and they degrade two-photon quantum interference visibility measurements. Figure 13 shows a plot of two-photon quantum interference measurements at low pump power (0.1 mW). The measurements, which were taken without subtracting accidental coincidences, yielded a visibility of 99.8% in the  $H$ - $V$  basis and 98.1% in the  $\pm 45^\circ$  ( $A/D$ ) basis. At higher pump powers, however, we observed that the visibility dropped, due to multi-pair events, with the visibility value being approximately equal to  $1-\alpha$ , where  $\alpha$  is the mean pair-generation rate per pulse

In addition to using PPKTP as the nonlinear crystal, we have been investigating a source based on the more efficient PPLN crystal pumped at 532 nm and with outputs at  $\sim 0.8$  and  $\sim 1.6$   $\mu\text{m}$ . This nondegenerate source is to be fiber coupled for improved spatial mode quality and for ease of transport. For the fiber-coupled downconverter it is necessary to focus the pump tightly to generate outputs that are in a single spatial mode. In preliminary testing we have focused the green pump to a spot size of 23  $\mu\text{m}$ , which has a confocal parameter that matches the length of the 20-mm PPLN crystal. By measuring the output flux at 797 nm within a 0.11 nm bandwidth, we observed  $\sim 50\%$  of the output light was coupled into a single-mode optical fiber [16]. Assuming that the free-space to fiber coupling efficiency is only 70%, this implies that about 70% of the downconverter output is in a single spatial mode. Further improvements in pump focusing and fiber coupling should make for a simple and efficient source of high-quality fiber-coupled entangled photons that can be utilized in many quantum information processing tasks.

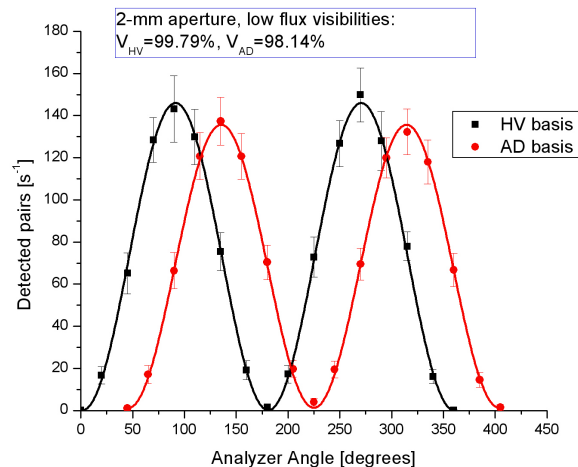


**Figure 13.** Two-photon quantum interference measurements in the  $H$ - $V$  basis and in the  $\pm 45^\circ$  ( $A/D$ ) basis. Downconverter was operated at low flux without appreciable multi-pair events.

Physical Simulation of the Entangling Probe BB84 Attack Fuchs and Peres [17] described the most general way in which an individual attack could be mounted against single-photon, polarization-based Bennett-Brassard 1984 quantum key distribution (BB84 QKD). Eve interacts a probe photon with Alice's photon in a unitary manner, then sends Alice's photon to Bob, and performs a probability operator-valued measurement on her probe photon. Slutsky *et al.* [18] demonstrated that the Fuchs-Peres construct — with the appropriate choice of probe state, interaction, and measurement — affords Eve the maximum amount of Rényi information about the error-free sifted bits that Bob receives for a given level of disturbance. Brandt [19] extended the Slutsky *et al.* treatment by showing that the optimal probe could be realized with a single controlled-NOT (CNOT) gate; see Fig. 14 for an abstract diagram of the resulting Fuchs-Peres-Brandt (FPB) probe. We have shown how a complete physical simulation of the FPB probe could be accomplished [20] using single-photon two-qubit (SPTQ) quantum logic [21,22]. Recently we

have performed a complete physical simulation of the FPB probe based on SPTQ quantum logic using the optical setup shown in Fig. 15 [23].

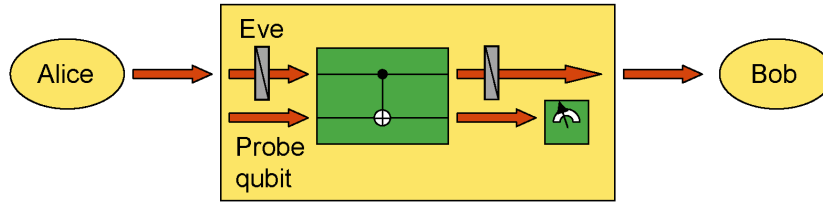


Figure 14. Fuchs-Peres-Brandt probe.

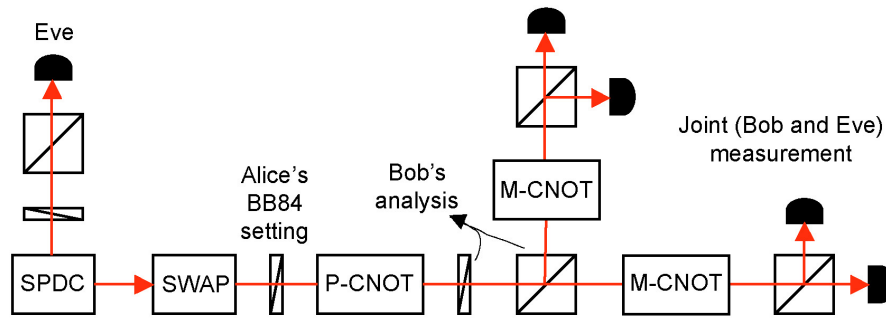
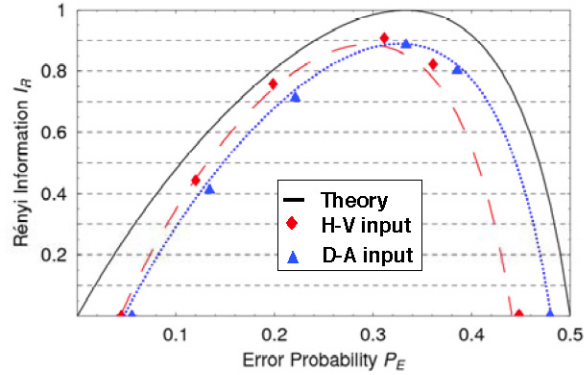


Figure 15. Physical simulation of the FPB probe.

We start with polarization-entangled photon pairs from our type-II phase matched Sagnac SPDC source [13]. Eve detects one of these photons, in a particular polarization, to both herald the presence of the other photon and determine its polarization. We then use an SPTQ SWAP gate to convert this polarization qubit into a momentum qubit, and follow that with a half-wave plate that Alice uses to set her BB84 polarization qubit. Our polarization-controlled-NOT (P-CNOT) gate then accomplishes the FPB probe interaction, with Alice's polarization qubit performing a CNOT on Eve's momentum qubit while both qubits are carried on the same photon. Another half-wave plate and a polarizing beam splitter then accomplish Bob's active polarization analysis. At this point we use two momentum-controlled-NOT (M-CNOT) gates, a pair of polarizing beam splitters, and four single-photon detectors to collect data that allow us to determine both Bob's and Eve's measurement results under an FPB-probe attack. Because this experiment requires Eve to be inside Bob's measurement apparatus, it represents a complete physical simulation, rather than a true implementation, of the FPB-probe attack. Nevertheless, its joint Alice-Bob-Eve measurement statistics equal those of the true attack, and the latter will be realizable once polarization-independent quantum nondemolition detection becomes available [20]. Our measurements with the Fig. 15 setup, shown in Fig. 16, are in good agreement with the theoretical values. In particular, the maximum information obtained by Eve (at ~90% in the experiment) occurs when the induced error probability is 1/3. The BB84 attack experiment offers a realistic physical simulation because it includes actual source and gate errors, as evidenced by the nonzero (~5%) error even if Eve receives no information (by setting the her probe qubit appropriately). The simulation apparatus can be especially useful for testing various privacy amplification protocols to ensure their validity and the functionality of the resulting secret key that the BB84 protocol generates.



**Figure 16.** Fuchs-Peres-Brandt probe measurement results for Alice's input in the  $H$ - $V$  and  $\pm 45^\circ$  ( $A/D$ ) bases, showing the Rényi information obtained by Eve as a function of the induced error probability that is detected by Alice and Bob. The measured results are in good agreement with theoretical values.

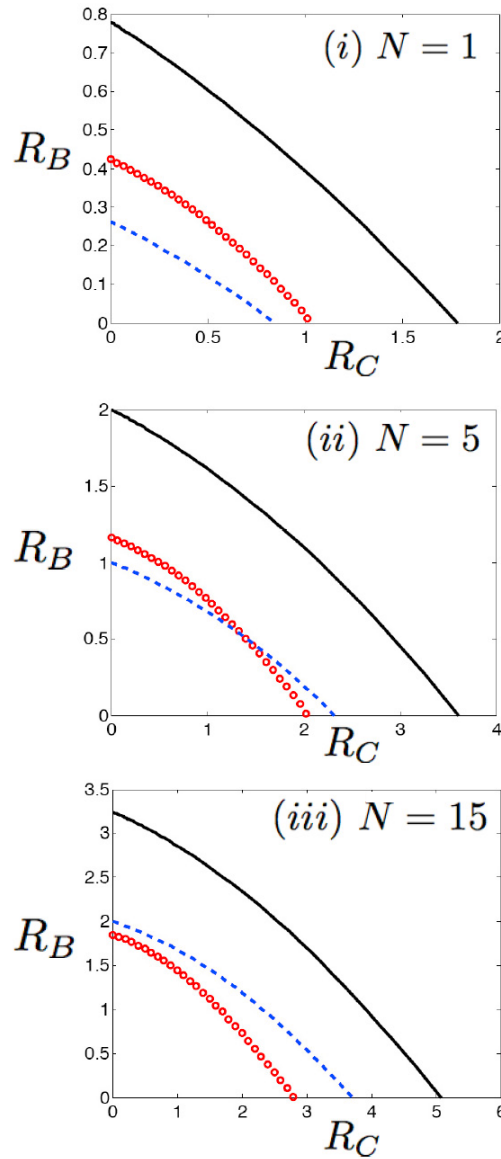
Classical Capacity of Free-Space Optical Communication The past decade has seen several advances in evaluating classical information capacities of several important quantum communication channels [24-29]. Despite these advances, exact capacity results are not known for many important and practical communication channels. We have been working to advance the line of research aimed at evaluating capacities of bosonic communication channels, which began with the capacity derivation for the input photon-number constrained lossless bosonic channel [26,27]. The capacity of the lossy bosonic channel was found in [28], where it was shown that a modulation scheme using classical light (coherent states) suffices to achieve ultimate communication rates over this channel. Subsequent attempts to evaluate the capacity of the lossy bosonic channel with additive Gaussian noise [29] led to a crucial conjecture on the minimum output entropy of a class of bosonic channels [30]. Proving that conjecture would complete the capacity proof for the bosonic channel with additive Gaussian noise, and it would show that this channel's capacity is achievable with classical-light modulation. More recent work that addressed bosonic multiple-access communication channels [31] revealed that modulation of information using non-classical states of light is necessary to achieve ultimate single-user rates in the multiple-access scenario.

During the past year we have made substantial progress in assessing the classical information capacity of the bosonic broadcast channel [32,33]. A broadcast channel is the congregation of communication media connecting a single transmitter to two or more receivers. In general, the transmitter encodes and sends out independent information to each receiver in a way that each receiver can reliably decode its respective information. We have shown that when coherent-state encoding is employed in conjunction with coherent detection, the bosonic broadcast channel is equivalent to a classical Gaussian broadcast channel whose capacity region is known, and known to be dual to that of the classical Gaussian multiple-access channel [34]. Thus, under these coding and detection assumptions, the capacity region of the bosonic broadcast channel is dual to that of the multiple-access bosonic channel with coherent-state encoding and coherent detection. To treat more general transmitter and receiver conditions, we have used a limiting argument to apply the degraded quantum broadcast-channel coding theorem for finite-dimensional state spaces [35] to the infinite-dimensional bosonic channel with an average photon-number constraint. We have considered the two-receiver case in which Alice ( $A$ ) simultaneously transmits to Bob ( $B$ ), via the transmissivity  $\eta > 1/2$  port of a lossless beam splitter, and to Charlie ( $C$ ), via that beam splitter's reflectivity  $1-\eta < 1/2$  port, using arbitrary encoding and optimum measurement with an average photon number  $N$  at the input. Given a new conjecture about the minimum output entropy of a lossy bosonic channel, we have shown that the ultimate capacity region is achieved by coherent-state encoding, and is given (in nats per channel use) by

$$R_B \leq g(\eta\beta N), R_C \leq g((1-\eta)N) - g((1-\eta)\beta N), \text{ for } 0 \leq \beta \leq 1,$$

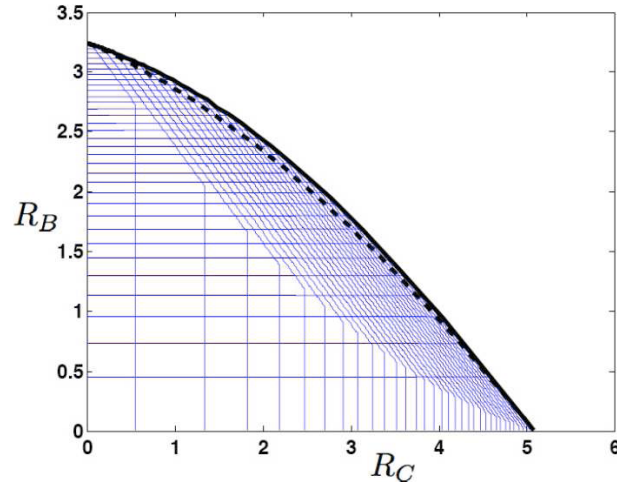
where  $g(x) = (x+1)\ln(x+1) - x\ln(x)$  is the Shannon entropy of the Bose-Einstein probability distribution with mean  $x$ .

Figure 17 compares the preceding conjectured capacity region — which we know to be the broadcast channel's capacity region when coherent-state encoding is employed — with those achieved by coherent-state encoding and coherent (homodyne and heterodyne) detection [33]. For these examples see that the conventional reception techniques fall substantially below the ultimate limits on reliable broadcast communications.



**Figure 17.** Comparison of bosonic broadcast channel capacity regions, in bits per channel use, achieved by coherent-state encoding with homodyne detection (the capacity region lies inside the boundary marked by circles), heterodyne detection (the capacity region lies inside the region bounded by dashes), and optimum reception (the capacity region lies inside the region bounded by the solid curve), for  $\eta = 0.8$  and  $N = 1, 5,$  and  $15$ .

Figure 18 shows that, unlike the classical case, the capacity region of the bosonic broadcast channel with coherent-state encoding and optimum reception is not the dual of the bosonic multiple-access channel with coherent-state encoding and optimum reception [33]. This figure shows that with a fixed beam splitter and identical average photon number budgets, more collective classical information can be sent when the beam splitter is used as a multiple-access channel as opposed to when it is used as a broadcast channel if coherent-state encoding is employed.



**Figure 18.** Comparison of bosonic broadcast and multiple-access channel capacity regions, in bits per channel use, for  $\eta = 0.8$  and  $N = 15$  with coherent-state encoding. The dashed curve is the outer boundary of the broadcast channel capacity region. It lies below the solid curve, which is the outer envelope of the multiple-access capacity regions.

We are continuing work on the broadcast channel by seeking a proof for the new minimum output entropy conjecture. So far, we have shown that the conjecture is true when Wehrl entropy is employed instead of von Neumann entropy [33]. We have also shown that our new minimum output entropy conjecture is equivalent to the prior one — associated with the lossy bosonic channel with additive Gaussian noise — when the input states are restricted to be Gaussian [33]. Moreover, in the Gaussian-input case, both conjectures are true.

Imaging with Phase-Sensitive Light We have been exploring the use of phase-sensitive light in a variety of imaging scenarios. A pair of Gaussian-state light beams that possess a phase-sensitive cross-correlation can be produced by continuous-wave (cw) spontaneous parametric downconversion (SPDC) with vacuum-state signal and idler inputs [13,36]. The low-flux limit of cw SPDC can then be approximated by a vacuum state plus a frequency-entangled biphoton. Many quantum imaging scenarios have been characterized — both theoretically and experimentally — in terms of post-selected biphoton detection, e.g., quantum optical coherence tomography [37,38], and ghost imaging [39]. The primary objective of our work has been to clearly delineate the boundary between classical and quantum behavior in these and other imaging scenarios and to use this understanding to develop new, and more robust imaging schemes that offer advantages over classical techniques. What follows is a brief summary of our results on optical coherence tomography and ghost imaging.

Optical coherence tomography (OCT) produces 3-D imagery through focused-beam scanning (for transverse resolution) and interference measurements (for axial resolution). Conventional OCT (C-OCT) uses classical-state signal and reference beams, with a phase-insensitive cross-correlation, and measures their second-order interference in a Michelson interferometer [34]. Quantum OCT (Q-OCT) employs signal and reference beams in an entangled biphoton state, and

measures their fourth-order interference in a Hong-Ou-Mandel (HOM) interferometer [37,38]. In comparison to C-OCT, Q-OCT offers the advantages of a two-fold improvement in axial resolution and even-order dispersion cancellation. Q-OCT's advantages have been ascribed to the non-classical nature of the entangled biphoton state, but we have shown that is the phase-sensitive cross-correlation between the signal and reference fields, rather than non-classical behavior *per se*, that provides the axial resolution improvement and even-order dispersion cancellation [41]. Based on this understanding, we have proposed a new OCT configuration — phase-conjugate OCT (PC-OCT) — which can exploit classical signal and reference beams with phase-sensitive cross-correlation to achieve the factor-of-two axial resolution improvement and the even-order dispersion cancellation reaped by Q-OCT. PC-OCT, shown schematically in Fig. 19, employs a double-pass interrogation of the sample being imaged — with a conjugate amplifier sandwiched in between these interrogations — followed by a Michelson interferometer measurement module as used in C-OCT. The conjugate amplifier converts the phase-sensitive cross-correlation between signal and reference into a phase-insensitive cross-correlation that can be sensed with the Michelson (second-order) interferometer. Q-OCT, on the other hand, needs a Hong-Ou-Mandel (fourth-order) interferometer, in order to measure phase-sensitive cross-correlation. Unlike Q-OCT, PC-OCT can use strong fields, hence it may be applicable to standoff sensing as well as microscopy.

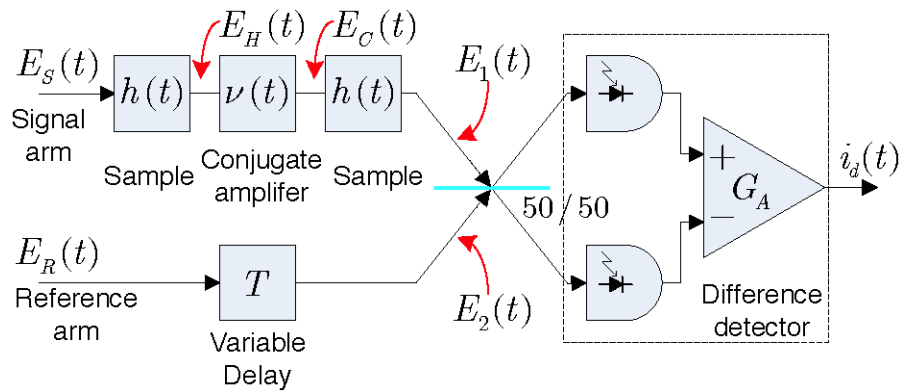


**Figure 19.** Schematic for phase-conjugate optical coherence tomography. The signal and reference are broadband light beams with a phase-sensitive cross correlation. The signal is transmitted to a target represented by a linear time-invariant filter  $h(t)$  — shown here in transmission, but in the real application it would be seen in reflection — and then phase conjugated upon its return in a parametric device with impulse response  $\nu(t)$ . The conjugate beam re-interrogates the target after which it is interfered with the delayed reference in a Michelson interferometer. Axial information is derived from the location of peak fringe visibility.

Ghost imaging is the acquisition of the transmittance pattern of an object through intensity correlation measurements, and it has been demonstrated with both thermal (classical) light and biphoton (quantum) light [39,42]. Recently, we have used our coherence theory [43] for Gaussian-state sources — which encompasses both thermal light and biphoton-state light as special cases — to show that almost all the characteristics of quantum ghost imaging are due to the phase-sensitive cross correlation between the signal and reference beams [44]. The particular ghost-imaging setup that we considered is shown in Fig. 20. For this arrangement we showed that thermal light, classical phase-sensitive light, and quantum phase-sensitive light all yield ghost images in both near-field and far-field operation. The same image inversion that has been seen in the quantum phase-sensitive light case, but not the thermal light case, turns out to be present for ghost imaging with classical phase-sensitive light. If the ghost-imager's source fields are constrained to have specific phase-insensitive auto-correlations, then quantum light offers a spatial resolution advantage in the source's near field and improved field-of-view in the far field. The principal advantage of quantum ghost imaging, however, comes from the near-absence of any background term in the ghost image.

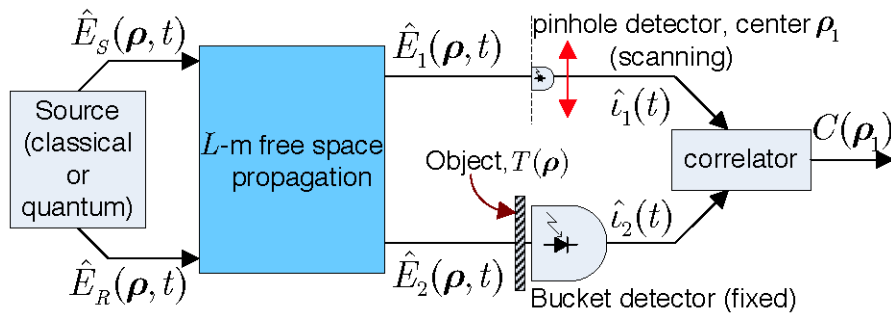


**Figure 20.** Schematic for ghost imaging. The signal and reference are broadband light beams with either a phase-insensitive or phase-sensitive cross correlation. After propagation over an  $L$ -m-long free space path, the signal beam illuminates a scanning pinhole detector and the reference illuminates an object transmittance mask followed by a large-area (bucket) detector. Cross correlating the resulting (shot-noise limited) photocurrents as the pinhole detector is scanned yields the ghost image.

## 2. Nonlinear Optics and Precision Measurements

### Sponsor

Office of Naval Research - Contract N00014-02-1-0717

### Project Staff

Professor Jeffrey H. Shapiro, Dr. Franco N. C. Wong, Dr. Dmitry Kolker

In an era that is increasingly technology driven, precision measurements play a key role in many areas of science and commerce, such as the very successful Global Positioning System (GPS). The recent introduction of femtosecond frequency-comb technology bridges the two extremes of time scales: ultrafast optics in the femtosecond regime and optical frequency metrology at the Hertz and sub-Hertz levels. One significant consequence is the functionality and simplicity afforded by femtosecond technology for use in precision measurements, such as the determination of absolute optical frequencies. We are working in collaboration with Professors Erich Ippen and Franz Kärtner to investigate enabling femtosecond-comb technologies with nonlinear optical techniques.

The main focus of our program is to apply nonlinear optical techniques to improve both the signal-to-noise ratio and stability of self-frequency referencing techniques and to facilitate new applications of femtosecond-comb technology for enhanced functionality. The technique of quasi-phase matching and the availability of multiple gratings in a single PPLN crystal offer flexibility in achieving multiple interactions by allowing each nonlinear process to take place in its own grating section. Back-to-back difference-frequency generation in a dual-grating PPLN chip has been used to achieve optical frequency division by 3 [45]. We have also realized self-phase locking in a divide-by-3 optical parametric oscillator (OPO) using a dual-grating PPLN chip in a triply resonant cavity [46].

More recently, we have taken the concept of multiple interactions to a new level of flexibility and tunability in a convenient setup. First we incorporated a fan-out grating section in a dual-grating PPLN chip. The phase matching of the uniform-grating first section is tunable by temperature. The interaction in the second section is tunable by a simple translation of the chip across the variable-period grating without affecting the first-section phase matching. We have utilized this dual-grating design to demonstrate a tunable cascaded OPO in a cavity that is resonant at all generated frequencies [47]. Pumped at 532 nm, the first grating generates the primary OPO while the secondary OPO is internally pumped by the primary signal field. We have

experimentally demonstrated wide tunability of 200 nm in the secondary OPO outputs by translating across the fan-out section.

In the past year, we have utilized the ease and tunability of the same dual-grating PPLN OPO setup to investigate self-phase locking in a divide-by-3 OPO. Unlike our previous divide-by-3 OPO, which employed a less flexible dual-grating PPLN chip and was pumped at 844 nm [46], our new OPO setup used a 532 nm continuous-wave (cw) pump laser and generated outputs at 798 and 1596 nm. These output wavelengths are conveniently located for detection by standard photodiodes and, more importantly, for linking to femtosecond combs in the Ti:sapphire laser region and in the telecommunication band.

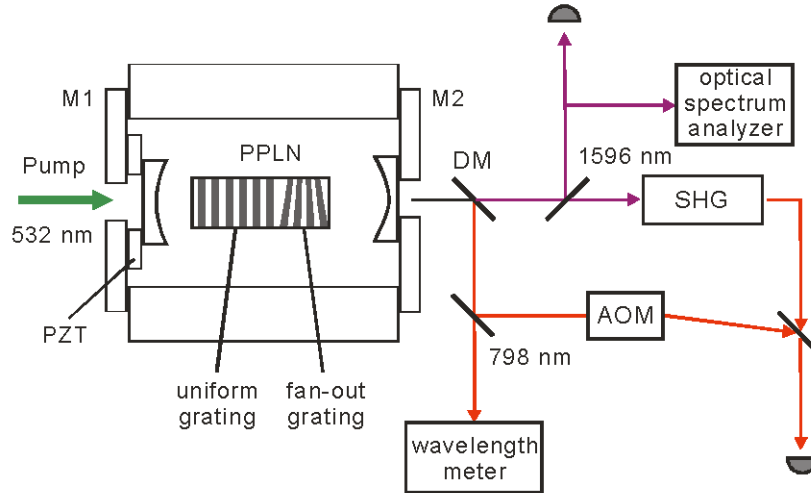


**Figure 21.** Schematic of the experimental setup. Doubly-resonant OPO cavity generates outputs at 798 and 1596 nm using a dual-grating PPLN chip. The 1596-nm idler signal is frequency doubled and mixed with the 80-MHz shifted 798-nm signal for monitoring the resultant beat note. DM, dichroic mirror; SHG, second-harmonic generator; AOM, acousto-optic modulator; PZT, piezoelectric transducer.

Figure 21 shows the schematic of the experimental setup. We used a 20-mm-long PPLN crystal with a 13-mm first section of  $7.2 \mu\text{m}$  grating period that could be phase matched for nondegenerate OPO outputs at  $\sim 0.8$  and  $\sim 1.6 \mu\text{m}$ . The PPLN temperature was typically set around  $204^\circ\text{C}$  that was found to be near the 3-to-1 operating point. The PPLN chip had a 7-mm second section with a fan-out grating structure that varied from  $19.45$  to  $19.85 \mu\text{m}$  over the 10-mm width of the crystal. At a fixed temperature, the PPLN chip could be translated along its width to access different grating periods of the fan-out section without changing the phase-matching condition for the OPO. The fan-out structure was used for phase-matched frequency doubling of the 1596-nm idler to yield an output that was close to the 798-nm signal. Self-phase locking for the OPO should occur when the frequency-doubled idler and the signal come within the OPO's locking range (tens of MHz).

In order to verify that the OPO is indeed self-phase locked at the exact divide-by-3 operating point, we used the setup shown in Fig. 21 to measure the beat note between the signal output and an externally frequency-doubled idler output. The 1596-nm idler output was externally frequency doubled in a 20-mm-long PPLN crystal and the resultant output at 798 nm was mixed with the 798-nm OPO signal output that was frequency shifted by 80 MHz using an acousto-optic modulator (AOM). The AOM frequency shift allowed the beat note to be easily observed on a radio-frequency spectrum analyzer. We have yet to observe a beat note definitively indicating stable self-phase locking operation. This may be due either to insufficient beat note signal strength or to our inability to tune within the self-phase locking range. However, we have

observed a beat note of 110 MHz between the 798-nm OPO signal and the internally frequency doubled OPO idler. The observed internal beat note suggests that the self-phase locking range is less than 110 MHz and that we did not have fine tuning capability to move closer to the exact 3-to-1 operating point. Part of the problem is that our 532-nm pump laser is not tunable and tuning can only be achieved by changing the phase matching conditions of the dual-grating PPLN chip.

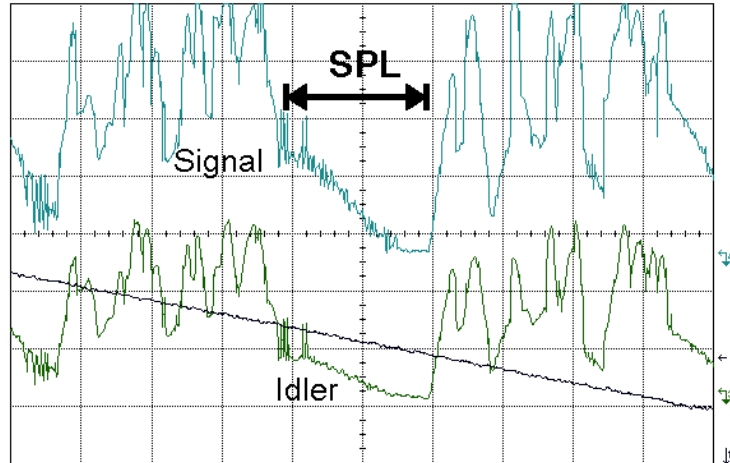


**Figure 22.** Signal (upper blue curve) and idler (lower green curve) outputs versus OPO cavity scanning. Absence of mode jumps indicates the OPO was in self-phase locking (SPL) regime. Operating temperature: 204°C.

We have, however, observed telltale signs of self-phase locking, as shown in Fig. 22. By scanning the OPO cavity length, we observed that sometimes the OPO did not make any mode hops over an extended scanning range, indicating the mode remained the same. This usually happens when the OPO is under self-phase locking condition, as detailed in our previous 3-to-1 self-phase locking work [46]. We are currently working to improve the OPO fine frequency tunability to achieve stable self-phase locking that can be verified with an external beat note measurement. A self-phase locked 3-to-1 OPO is particularly interesting because its three frequency markers can be utilized to phase lock two femtosecond frequency combs in different spectral regions to form a single multi-octave frequency comb for precision frequency metrology applications.

## References

1. J. H. Shapiro, "Architectures for Long-Distance Quantum Communication," *New J. Phys.* 4, 47 (2002).
2. S. Lloyd, J. H. Shapiro, F. N. C. Wong, P. Kumar, S. M. Shahriar, and H. P. Yuen, "Infrastructure for the Quantum Internet," *ACM SIGCOMM Comp. Commun. Rev.* 34, 9-20 (2004).
3. C. H. Bennett, G. Brassard, C. Crépeau, R. Jozsa, A. Peres, and W. K. Wootters, "Teleporting and Unknown Quantum State via Dual Classical and Einstein-Podolsky-Rosen Channels," *Phys. Rev. Lett.* 70, 1895-1899 (1993).
4. S. Lloyd, M. S. Shahriar, J. H. Shapiro, and P. R. Hemmer, "Long-Distance Unconditional Teleportation of Atomic States via Complete Bell State Measurements," *Phys. Rev. Lett.* 87, 167903 (2001).

5. J. H. Shapiro and N. C. Wong, "An Ultrabright Narrowband Source of Polarization-Entangled Photon Pairs," *J. Opt. B: Quantum Semiclass. Opt.* 2, L1-L4 (2000).
6. B. J. Yen and J. H. Shapiro, "Error Models for Long-Distance Qubit Teleportation," *IEEE J. Sel. Topics in Quantum Electron.* 9, 1483-1494 (2003).
7. M. Razavi, "Long-Distance Quantum Communication with Neutral Atoms," Ph.D. thesis, Department of Electrical Engineering and Computer Science, MIT 2006; also Res. Lab. Electron. Technical Rep. 719.
8. M. Razavi and J. H. Shapiro, "Nonadiabatic Approach to Entanglement Distribution over Long Distances," *Phys. Rev. A* 73, 032318 (2007).
9. M. Fleischhauer, S. F. Yelin, and M. D. Lukin, "How to Trap Photons? Storing Single-Photon Excitations in Collective Atomic Excitations," *Opt. Commun.* 179, 395-410 (2000).
10. P. G. Kwiat, E. Waks, A. G. White, I. Appelbaum, and P. H. Eberhard, "Ultrabright Source of Polarization-Entangled Photons," *Phys. Rev. A* 60, R773-R776 (1999).
11. T. Kim, M. Fiorentino, and F. N. C. Wong, "Phase-Stable Source of Polarization-Entangled Photons using a Polarization Sagnac Interferometer," *Phys. Rev. A* 73, 012316 (2006).
12. M. Fiorentino, G. Messin, C. E. Kuklewicz, F. N. C. Wong, and J. H. Shapiro, "Generation of Ultrabright Tunable Polarization Entanglement without Spatial, Spectral or Temporal Constraints," *Phys. Rev. A* 69, 041801(R) (2004).
13. F. N. C. Wong, J. H. Shapiro, and T. Kim, "Efficient Generation of Polarization-Entangled Photons in a Nonlinear Crystal," *Laser Phys.* 16, 1517-1524 (2006).
14. J. F. Clauser, M. A. Horne, A. Shimony, and R. A. Holt, "Proposed Experiment to Test Local Hidden-Variable Theories," *Phys. Rev. Lett.* 23, 880-884 (1969).
15. O. Kuzucu, F. N. C. Wong, D. E. Zelmon, S. M. Hegde, T. D. Roberts, and P. Battle, "Generation of 250 mW Narrowband Pulsed Ultraviolet Light by Frequency Quadrupling of an Amplified Erbium-doped Fiber Laser," *Opt. Lett.* 32, 1290-1292 (2007).
16. D. Venkatraman, "Tools for Quantum Optics: Pulsed Polarization-Maintaining Er-doped Fiber Laser and Spatial Mode Manipulation in Spontaneous Parametric Downconversion," M.Eng. thesis, Department of Electrical Engineering and Computer Science, MIT 2007.
17. C. A. Fuchs and A. Peres, "Quantum-State Disturbance versus Information Gain: Uncertainty Relations for Quantum Information," *Phys. Rev. A* 53, 2038-2045 (1996).
18. B. A. Slutsky, R. Rao, P.-C. Sun, and Y. Fainman, "Security of Quantum Cryptography against Individual Attacks," *Phys. Rev. A* 57, 2383-2398 (1998).
19. H. E. Brandt, "Quantum-Cryptographic Entangling Probe," *Phys. Rev. A* 71, 042312 (2005).
20. J. H. Shapiro and F. N. C. Wong, "Attacking Quantum Key Distribution with Single-Photon Two-Qubit Quantum Logic," *Phys. Rev. A* 73, 012315 (2006).
21. M. Fiorentino and F. N. C. Wong, "Deterministic Controlled-NOT Gate for Single-Photon Two-Qubit Quantum Logic," *Phys. Rev. Lett.* 93, 070502 (2004).
22. M. Fiorentino, T. Kim, and F. N. C. Wong, "Single-Photon Two-Qubit SWAP Gate for Entanglement Manipulation," *Phys. Rev. A* 72, 012318 (2005).

23. T. Kim, I. Stork genannt Wersborg, F. N. C. Wong, and J. H. Shapiro, "Complete Physical Simulation of the Entangling-Probe Attack on the Bennett-Brassard 1984 Protocol," *Phys. Rev. A* 75, 042327 (2007).
24. C. H. Bennett and P. W. Shor, "Quantum Information Theory," *IEEE Trans. Information Theory* 44, 2724-2742 (1998).
25. M. Nielsen and I. L. Chuang, *Quantum Computation and Quantum Information* (Cambridge University Press, Cambridge, 2000).
26. H. P. Yuen and M. Ozawa, "Ultimate Information Carrying Limit of Quantum Systems," *Phys. Rev. Lett.* 70, 363-366 (1993).
27. C. M. Caves and P. D. Drummond, "Quantum Limits on Bosonic Communication Rates," *Rev. Mod. Phys.* 66, 481-537 (1994).
28. V. Giovannetti, S. Guha, S. Lloyd, L. Maccone, J. H. Shapiro, and H. P. Yuen, "Classical Capacity of the Lossy Bosonic Channel: the Exact Solution," *Phys. Rev. Lett.* 92, 027902 (2004).
29. V. Giovannetti, S. Guha, S. Lloyd, L. Maccone, J. H. Shapiro, B. J. Yen, and H. P. Yuen, "Classical Capacity of Free-Space Optical Communication," in *Quantum Information, Statistics, Probability* ed. O. Hirota (Rinton Press, New Jersey, 2004).
30. V. Giovannetti, S. Guha, S. Lloyd, L. Maccone, and J. H. Shapiro, "Minimum Output Entropy of Bosonic Channels: a Conjecture," *Phys. Rev. A* 70, 032315 (2004).
31. B. J. Yen and J. H. Shapiro, "Multiple-Access Bosonic Communications," *Phys. Rev. A* 72, 062312 (2005).
32. S. Guha and J. H. Shapiro, "Bosonic Broadcast Channel Capacity and a New Minimum Output Entropy Conjecture," *Proceedings of the Eighth International Conference on Quantum Communication, Measurement and Computing*, Tsukuba, Japan, November 28 – December 3, 2006.
33. S. Guha, J. H. Shapiro, and B. I. Erkmen, "Classical Capacity of Bosonic Broadcast Communication and a Minimum Output Entropy Conjecture," *Phys. Rev. A*, forthcoming (2007).
34. N. Jindal, S. Vishwanath, and A. Goldsmith, "On the Duality of Gaussian Multiple-Access and Broadcast Channels," *IEEE Trans. Inform. Theory* 50, 768-783 (2004).
35. J. Yard, P. Hayden, and I. Devetak, "Quantum Broadcast Channels," e-print quant-ph/0603098.
36. J. H. Shapiro and K.-X. Sun, "Semiclassical versus Quantum Behavior in Fourth-Order Interference," *J. Opt. Soc. Am. B* 11, 1130-1141 (1994).
37. A. F. Abouraddy, M. B. Nasr, B. E. A. Saleh, A. V. Sergienko, and M. C. Teich, "Quantum Optical Coherence Tomography with Dispersion Cancellation," *Phys. Rev. A* 65 053817 (2002).
38. M. B. Nasr, B. E. A. Saleh, A. V. Sergienko, and M. C. Teich, "Demonstration of Dispersion-Canceled Quantum-Optical Coherence Tomography," *Phys. Rev. Lett.* 91, 083601 (2003).

39. T. B. Pittman, Y. H. Shih, D. V. Strekalov, and A. V. Sergienko, "Optical Imaging by Means of Two-Photon Quantum Entanglement," *Phys. Rev. A* 52, R3429-R3432 (1995).
40. J. M. Schmitt, "Optical Coherence Tomography: A Review," *J. Sel. Top. In Quantum Electron.* 5, 1205-1215 (1999).
41. B. I. Erkmen and J. H. Shapiro, "Phase-Conjugate Optical Coherence Tomography," *Phys. Rev. A* 74, 041601(R) (2006).
42. F. Ferri, D. Magatti, A. Gatti, M. Bache, E. Brambilla, and L. A. Lugiato, "High Resolution Ghost Image and Ghost Diffraction Experiments with Thermal Light," *Phys. Rev. Lett.* 94, 183602 (2005).
43. B. I. Erkmen and J. H. Shapiro, "Optical Coherence Theory for Phase-Sensitive Light," *Proc. SPIE* 6305, 6305G (2006).
44. B. I. Erkmen and J. H. Shapiro, "Ghost Imaging: What is Quantum, What is not," submitted to *Phys. Rev. Lett.*; eprint quant-ph/0612070.
45. P. T. Nee and N. C. Wong, "Optical Frequency Division by 3 of 532 nm in Periodically Poled Lithium Niobate with a Double Grating," *Opt. Lett.* 23, 46-48 (1998).
46. J.-J. Zondy, D. Kolker, and F. N. C. Wong, "Dynamical Signatures of Self-Phase-Locking in a Triply Resonant Optical Parametric Oscillator," *Phys. Rev. Lett.* 93, 043902 (2004).
47. P. V. Gorelik, F. N. C. Wong, D. Kolker, J.-J. Zondy, "Cascaded Optical Parametric Oscillation with a Dual-Grating Periodically Poled Lithium Niobate Crystal," *Opt. Lett.* 31, 2039-2041 (2006).

## Publications

### Journal Articles, Published

- B. I. Erkmen and J. H. Shapiro, "Phase-Conjugate Optical Coherence Tomography," *Phys. Rev. A* 74, 041601(R) (2006).
- C. E. Kuklewicz, F. N. C. Wong, and J. H. Shapiro, "Time-Bin Modulated Biphotons from Cavity-Enhanced Down-Conversion," *Phys. Rev. Lett.* 97, 223601 (2006).
- F. N. C. Wong, J. H. Shapiro, and T. Kim, "Efficient Generation of Polarization-Entangled Photons in a Nonlinear Crystal," *Laser Phys.* 16, 1517-1524 (2006).
- M. Razavi and J. H. Shapiro, "Nonadiabatic Approach to Entanglement Distribution over Long Distances," *Phys. Rev. A* 75, 032318 (2007).
- T. Kim, I. Stork genannt Wersborg, F. N. C. Wong, and J. H. Shapiro, "Complete Physical Simulation of the Entangling-Probe Attack on the Bennett-Brassard 1984 Protocol," *Phys. Rev. A* 75, 042327 (2007).
- J. Kim, J. Chen, Z. Zhang, F. N. C. Wong, F. X. Kärtner, F. Loehl, and H. Schlarb, "Long-Term Femtosecond Timing Link Stabilization using a Single-Crystal Balanced Cross Correlator," *Opt. Lett.* 32, 1044-1046 (2007).

## Chapter 41. Optical and Quantum Communications

O. Kuzucu, F. N. C. Wong, D. E. Zelmon, S. M. Hegde, T. D. Roberts, and P. Battle, "Generation of 250 mW Narrowband Pulsed Ultraviolet Light by Frequency Quadrupling of an Amplified Erbium-doped Fiber Laser," *Opt. Lett.* 32, 1290–1292 (2007).

J. H. Shapiro and M. Razavi, "Continuous-Time Cross-Phase Modulation and Quantum Computation," *New J. Phys.* 9, 16 (2007)

### **Journal Articles, Accepted for Publication**

S. Guha, J. H. Shapiro, and B. I. Erkmen, "Classical Capacity of Bosonic Broadcast Communication and a Minimum Output Entropy Conjecture," *Phys. Rev. A*, forthcoming (2007).

J. H. Shapiro and F. N. C. Wong, "On-Demand Single-Photon Generation using a Modular Array of Parametric Downconverters with Electro-Optic Polarization Controls," *Opt. Lett.*, forthcoming (2007).

### **Journal Articles, Submitted for Publication**

B. I. Erkmen and J. H. Shapiro, "Ghost Imaging: What is Quantum, What is not," submitted to *Phys. Rev. Lett.*; eprint quant-ph/0612070.

### **Meeting Papers, Published**

B. I. Erkmen and J. H. Shapiro, "Optical Coherence Theory for Phase-Sensitive Light," *Proc. SPIE* 6305, 6305G (2006).

B. I. Erkmen and J. H. Shapiro, "Optical Coherence Tomography with Phase-Sensitive Light," *Proc. SPIE* 6305, 630510 (2006).

S. Guha and J. H. Shapiro, "Bosonic Broadcast Channel Capacity and a New Minimum Output Entropy Conjecture," *Proceedings of the Eighth International Conference on Quantum Communication, Measurement and Computing*, Tsukuba, Japan, November 28 - December 3, 2006.

J. H. Shapiro and M. Razavi, "Continuous-Time Cross-Phase Modulation and Quantum Computation," *Proceedings of the Eighth International Conference on Quantum Communication, Measurement and Computing*, Tsukuba, Japan, November 28 - December 3, 2006.

F. N. C. Wong, T. Kim, C. E. Kuklewicz, O. Kuzucu, M. Fiorentino, J. H. Shapiro, and M. A. Albota, "A Toolbox for Photonic Entanglement Generation: Ultrabright, Ultranarrowband, and Ultrafast," *Proceedings of the Eighth International Conference on Quantum Communication, Measurement and Computing*, Tsukuba, Japan, November 28 - December 3, 2006.

T. Kim, I. Stork genannt Wersborg, F. N. C. Wong, and J. H. Shapiro, "Experimental Realization of Entangling-Probe Attack on the BB84 Protocol," *Proceedings of the Eighth International Conference on Quantum Communication, Measurement and Computing*, Tsukuba, Japan, November 28 - December 3, 2006.

O. Kuzucu, F. N. C. Wong, D. E. Zelmon, S. M. Hegde, T. D. Roberts, and P. Battle, "Frequency Quadrupled Picosecond Fiber Laser for UV Generation," *Digest of Advanced Solid State Photonics*, Vancouver, Canada, January 28-31, 2007.

J. Kim, F. Löhl, J. Chen, Z. Zhang, H. Schlarb, F. Wong, and F. Kärtner, "Long-Term Femtosecond Timing Link Stabilization using a Single-Crystal Balanced Cross-Correlator," *Digest of Conference on Lasers and Electro-Optics*, Baltimore, MD, May 7-11, 2007.

O. Kuzucu, F. N. C. Wong, D. E. Zelmon, S. M. Hegde, T. D. Roberts, and P. Battle, "Pulsed Picosecond UV Source by Frequency Quadrupling," *Digest of Conference on Lasers and Electro-Optics*, Baltimore, MD, May 7-11, 2007.

T. Kim, I. Stork genannt Wersborg, F. N. C. Wong, and J. H. Shapiro, "Complete Physical Simulation of the Entangling-Probe Attack on the BB84 Protocol," *Digest of Quantum Electronics and Laser Science Conference*, Baltimore, MD, May 7-11, 2007.

O. Kuzucu and F. N. C. Wong, "Narrowband Pulsed Polarization-Entangled Photon Source for Free-Space Quantum Key Distribution," *Digest of Quantum Electronics and Laser Science Conference*, Baltimore, MD, May 7-11, 2007.

M. Razavi and J. H. Shapiro, "Kerr-Induced Phase Noise in Quantum Parity Gates," *Digest of Quantum Electronics and Laser Science Conference*, Baltimore, MD, May 7-11, 2007.

J. H. Shapiro, "Quantum Pulse Compression Laser Radar," *Proc. SPIE* 6603, 660306 (2007).

D. Kolker, F. N. C. Wong, and J. J. Zondy, "Self-Phase Locking in a 3-to-1 Doubly-Resonant Dual-Grating Optical Parametric Oscillator," *International Conference on Coherent and Nonlinear Optics*, Minsk, Belarus, May 28 - June 1, 2007.

F. N. C. Wong, O. Kuzucu, and J. H. Shapiro, "High-Flux Pulsed Polarization-Entangled Photon Source for Generating Single Photons on Demand," *Proceeding of the Ninth Rochester Conference on Coherence and Quantum Optics*, Rochester, NY, June 10-13, 2007.

J. H. Shapiro and B. I. Erkmen, "Imaging with Phase-Sensitive Light," *Proceedings of the International Conference on Quantum Information*, Rochester, NY, June 13-15, 2007.

S. Guha and J. H. Shapiro, "Capacity of Bosonic Broadcast Channels," *Digest of the 2007 IEEE International Symposium on Information Theory*, Nice, France, June 24-29, 2007.

### Theses

M. Razavi, "Long-Distance Quantum Communication with Neutral Atoms," Ph.D. thesis, Department of Electrical Engineering and Computer Science, MIT 2006; also Res. Lab. Electron. Technical Rep. 719.

D. Venkatraman, *Tools for Quantum Optics: Pulsed Polarization-Maintaining Er-doped Fiber Laser and Spatial Mode Manipulation in Spontaneous Parametric Downconversion*, M.Eng. thesis, Department of Electrical Engineering and Computer Science, MIT 2007.

